

A new strategy for matching observed and simulated lensing galaxies

Philipp Denzel,^{1,2} * Sampath Mukherjee,³ Prasenjit Saha^{1,2}

¹*Institute for Computational Science, University of Zurich, CH-8057 Zurich, Switzerland*

²*Physics Institute, University of Zurich, CH-8057 Zurich, Switzerland*

³*STAR Institute, Quartier Agora - Allée du six Août, 19c B-4000 Liège, Belgium*

ABSTRACT

The study of strong-lensing systems conventionally involves constructing a mass distribution that can reproduce the observed multiply-imaging properties. Such mass reconstructions are generically non-unique. Here, we present an alternative strategy: instead of modelling the mass distribution, we search cosmological galaxy-formation simulations for plausible matches. In this paper we test the idea on seven well-studied lenses from the SLACS survey. For each of these, we first pre-select a few hundred galaxies from the EAGLE simulations, using the expected Einstein radius as an initial criterion. Then, for each of these pre-selected galaxies, we fit for the source light distribution, while using MCMC for the placement and orientation of the lensing galaxy, so as to reproduce the multiple images and arcs. The results indicate that the strategy is feasible, and even yields relative posterior probabilities of two different galaxy-formation scenarios, though these are not statistically significant yet. Extensions to other observables, such as kinematics and colours of the stellar population in the lensing galaxy, is straightforward in principle, though we have not attempted it yet. Scaling to arbitrarily large numbers of lenses also appears feasible. This will be especially relevant for upcoming wide-field surveys, through which the number of galaxy lenses will rise possibly a hundredfold, which will overwhelm conventional modelling methods.

Key words: gravitational lensing: strong — galaxies: formation — galaxies: evolution — methods: numerical

1 INTRODUCTION

Four decades after the first discovery by [Walsh et al. \(1979\)](#), galaxies exhibiting strong gravitational lensing seem almost commonplace. The SLACS sample (Sloan Lens ACS; [Bolton et al. 2006, 2008](#); [Shu et al. 2017](#)) alone has over a hundred strong lensing galaxies. The next generation of wide-field surveys (LSST/Rubin from the ground, and Euclid and WFIRST/RST in space) promise many many more. Extrapolation from small fields that have been surveyed at different resolutions indicate (see e.g., [Collett 2015](#)) that $> 100'000$ strong-lensing galaxies await discovery. Many techniques for finding lenses in surveys, ranging from crowdsourcing ([Marshall et al. 2016](#)) to neural networks (e.g., [Davies et al. 2019](#)), have been developed in recent years, and one can confidently expect that 10^5 strong-lensing galaxies will be discovered.

Meanwhile, the past decade has seen significant progress on the structure and formation of galaxies. Within the Λ CDM paradigm, there is general agreement regarding the growth of density perturbations under gravity, from the level observed in the cosmic microwave background to the formation of dark-matter halos. The subsequent processes of star formation and

the resultant feedback are less well understood and require sub-grid models to simulate, but still the galaxies formed in simulations like Illustris ([Vogelsberger et al. 2014](#)), FIRE (Feedback In Realistic Environments; [Hopkins et al. 2014](#)), and EAGLE (Evolution and Assembly of GaLaxies and their Environments; [Crain et al. 2015](#)) are much more credible than previous generations of simulated galaxies. The SEAGLE pipeline (Simulating EAGLE Lenses; [Mukherjee et al. 2018](#)) producing simulated lenses from EAGLE is of particular interest in this work. In addition to galaxy-formation simulations, there are also distribution-function models for galaxies, such as from AGAMA (action-based galaxy modelling architecture; [Vasiliev 2018](#)), which provide self-consistent phase-space distributions for dark matter, stars and gas.

One would like to compare lensing observations with galaxy simulations. Let us first consider this task in a rather abstract way. Let F be some galaxy-formation scenario, and let D represent the observational data. In Bayesian terms, the posterior probability of F after comparison with D would be

$$P(F|D) = \frac{P(D|F)P(F)}{P(D)} \quad (1)$$

where $P(F)$ represents the probability of F before the data,

* Email: phdenzel@physik.uzh.ch

and $P(D)$ is the probability of the data marginalized over all possible F . The factors $P(F)$ and $P(D)$ cancel if we compare two formation scenarios with equal prior probability, so it is really $P(D|F)$ that is of interest. This quantity is given by the marginalisation

$$P(D|F) = \sum_g P(D|g) P(g|F) \quad (2)$$

where g represents galaxy properties. There will also be nuisance parameters (call these ν), such as the orientation of the ellipticity of a galaxy, which are also to be marginalised over, thus

$$P(D|g) = \sum_\nu P(D|g, \nu) P(\nu). \quad (3)$$

Conventional lens modelling consists of constructing g so as to optimise $P(D|g)$. Here, there are two basic approaches. One is to assume some parametric form for the lensing mass distribution and fit to the data. The idea goes back to the very first lens-modelling paper (Young et al. 1980). Recent parametric lens models (such as Yildirim et al. 2020) are more elaborate, but still much simplified compared to a simulation from AGAMA or SEAGLE. Alternatively, one can let the lensing mass distribution be free-form, and sample the abstract space of mass distributions that fit the data. This approach is more common in cluster lensing (see e.g., Wagner et al. 2019), but also used in galaxy lensing (e.g., Küng et al. 2018). Free-form mass models are more complex, but they are not necessarily dynamically plausible. Neither style of lens modelling has much input from $P(g|F)$. Some comparisons of lens models against dynamical simulations of galaxies have been done (e.g. Saha et al. 2006; Barnabè et al. 2009; Coles et al. 2014; Ding et al. 2020), as have some model-independent comparisons of image statistics with substructure in Λ CDM (Gomer & Williams 2017), but all of these provide only qualitative information with respect to $P(g|F)$.

In this work, we attempt for the first time a direct comparison of lensing data and galaxy-formation without conventional lens models. We use SEAGLE lenses as samples of $P(g|F)$ from two different galaxy-formation scenarios. We then formulate $P(D|g, \nu)$ so that a procedure for fitting source brightness distributions (developed earlier for conventional lens modelling Denzel et al. 2020b; Denzel et al. 2020a) can be repurposed. This allows us to find EAGLE galaxies that can account for the observed images in a small test sample of seven SLACS lenses (see Table 1). As this work is intended as proof of concept, we do not include data other than multiple images from extended sources.

The following Section 2 introduces what we may call the $P(D|F)$ method. The subsequent Section 3 details the SEAGLE pipeline and summarizes how the catalogue of surface-density maps was compiled. The selected test-case lenses from the SLACS survey are presented in Section 4, and the results of these tests are reported in Section 5. Finally, a summary and discussion, in particular about possible expansions and applications of the lens-matching approach are given in Section 6.

2 THE PLAUSIBLE-MATCH METHOD

To go beyond the simple abstractions above and discuss the actual method, let us rewrite Eqs. (2) and (3) as

$$P(D|F) \approx \sum_{s, \xi} P(I^{\text{obs}} | \alpha, s) P(\alpha, | \xi, F) P(s, \xi). \quad (4)$$

Rather than galaxy properties g in general, we are concerned with a lensing deflection field α . The ν parameters consist of (a) location and rotation parameters (say ξ) to produce α from a simulated EAGLE galaxy, and (b) the unlensed brightness distribution s at the source redshift. The priors $P(s, \xi)$ we take as flat. Hence it is on the factors $P(D|\alpha, s)$ and $P(\alpha|\xi, F)$ that we must concentrate.

2.1 Data adaptation

We now describe the ingredients for the factor

$$P(\alpha, | \xi, F)$$

in Eq. (4).

The convergence map (that is, the lensing mass distribution in dimensionless form) is given by the usual projection of the 3D mass density as

$$\kappa(\theta, \xi) = \frac{4\pi G}{cH_0} \frac{d_{LS}d_L}{d_S} \int \rho(\theta, \xi, z) dz. \quad (5)$$

Here, θ is the angle on the observer's sky, d_{LS} is the dimensionless angular-diameter distance from the lens to the source, d_L and d_S are analogous, and ξ represents the location and orientation of the 3D density $\rho(\theta, z)$. A conventional Λ CDM cosmology is assumed.

In this work, we have limited the analysis to two galaxy-formation scenarios from the EAGLE simulations (details are in Section 3 below). From the two simulations, SEAGLE projected each of 554 simulated galaxies along three orthogonal axes to produce maps of $\kappa(\theta)$ for the fiducial redshift values $z_L = 0.23$ and $z_S = 0.8$. The κ maps have 161×161 square pixels with a pixel size of $0.05''$, yielding an angular size of about $8'' \times 8''$ for an entire map. The κ distributions differ in size and in shape. Figure 1 shows the distribution of mean enclosed κ as a function of radial distance from lens centre for the entire catalogue. The notional Einstein radius is the value of θ_E for which $\langle \kappa \rangle_{\theta_E} = 1$. About 20 mass maps in the catalogue are always below $\kappa = 1$ and hence are not strongly lensing for $z_L = 0.23, z_S = 0.8$. But most of the galaxies can produce multiple images, and the Einstein radii go up to $3.15''$.

The convergence maps are then rescaled from $z_L = 0.23, z_S = 0.8$ to the redshift values corresponding to each of the test-case lens system listed in Table 1. A subset of a few hundred κ maps with Einstein radius in the expected range for each system was then selected for further processing.

The next step was the computation of the lens potential $\psi(\theta) = 2\nabla^{-2}Q(\theta)$. To reduce the computational time required, the κ maps were discretised to 23×23 tiles. The potential is then expressed as

$$\psi(\theta) = 2 \sum_n \kappa_n \nabla^{-2} Q(\theta - \theta_n) \quad (6)$$

where κ_n is the density of the n -th tile and $Q(\theta - \theta_n)$ is the contribution of a square tile with constant $\kappa = 1$ located

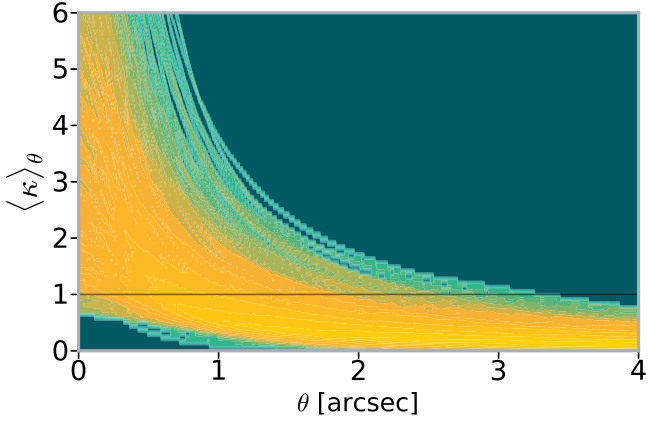


Figure 1. The distribution of radial profiles of the mean enclosed $\langle \kappa \rangle_\theta$ within a given projected radius from the centre of the galaxies, for the entire catalogue, assuming $z_L = 0.23, z_S = 0.8$. The horizontal line at $\kappa = 1$ indicates the notional Einstein radii.

at θ_n . The functional form of $Q(\theta)$ is given in [AbdelSalam et al. \(1998\)](#). Note that only the mass distribution is reduced in resolution in this way, but θ and $\psi(\theta)$ can still be evaluated at any desired resolution. The effect of the approximation (6) is expected to be very small.

Once the lens potential is known we have the deflection angle as

$$\alpha(\theta) = \nabla\psi(\theta). \quad (7)$$

2.2 Synthetic images

We now consider the factor $P(I^{\text{obs}} | \alpha, s)$ in Eq. (4).

As a result of the deflection (7) a light ray originating at a source at β on the sky will be observed at θ which is related to β by the usual lens equation

$$\beta = \theta - \alpha(\theta). \quad (8)$$

The lens equation amounts to a mapping $L(\theta, \beta)$ between the source and image planes, which can be discretised as a matrix. Any given θ corresponds to a unique β , whereas a given β may correspond to more than one θ . A source-brightness distribution $s(\beta)$ produces an image-brightness distribution

$$I(\theta) = \int L(\theta, \beta) s(\beta) d^2\beta. \quad (9)$$

The observed image brightness will involve a further convolution with the point-spread function (PSF) $P(\theta - \theta')$ of the telescope and camera. The result

$$\bar{I}(\theta) = \int P(\theta - \theta') I(\theta') d^2\theta' \quad (10)$$

we will call the synthetic image, and it is what will get compared with the data.

For the lens sample investigated here, appropriate PSFs have been employed which were modelled using `tinytim`¹ ([Krist et al. 2011](#)).

Assuming now that the detector noise is Gaussian with known $\sigma_\theta \propto \sqrt{I^{\text{obs}}(\theta)}$ we take

$$P(I^{\text{obs}} | \alpha, s) \propto \exp\left(-\frac{1}{2}\chi^2\right) \quad (11)$$

where

$$\chi^2 = \sum_{\theta} \sigma_\theta^{-2} \left[I^{\text{obs}}(\theta) - \bar{I}(\theta, \alpha, s) \right]^2 \quad (12)$$

From Eqs. (9) and (10) it is clear that the synthetic image $\bar{I}(\theta)$ is linear in the source-brightness distribution, even though it is completely non-linear in the mass distribution. Hence $s(\beta)$ can be solved to optimise $P(I^{\text{obs}} | \alpha, s)$ by linear least-squares. It is important, however, to mask the light from the lensing galaxy, since it is not part of $I^{\text{obs}}(\theta)$.

As the lensed images are typically highly magnified, the source or β plane needs much smaller pixels than the image or θ plane. For this reason, the lens mapping $L(\theta, \beta)$ maps each θ pixel to a cluster of β pixels. To simplify the computation, we replace each θ pixel by its central point for the purposes of the lens mapping. Then each image pixel maps to a single source pixel. This procedure leaves many source pixels ‘blank’, because they send light to edges and corners of the image pixels. These blank pixels could be filled in by interpolation, but in this paper we have not done so. As a result, the reconstructed sources have a fragmented appearance on small scales, as we will see later in Figs. 4–10.

While the fitting of synthetic images is essentially the same as in conventional lensing modelling (our implementation is the same as in [Denzel et al. 2020b](#); [Denzel et al. 2020a](#)), plausible-matching requires a further issue to be solved, namely the alignment and orientation of the lens system. The nuisance parameters $\xi = (p_{\text{rel}}, \phi_{\text{rel}})$, where p_{rel} is the position, ϕ_{rel} is the orientation of the mass map relative to the observation, needs to be marginalised out. The marginalisation is done using short Markov-Chain Monte-Carlo (MCMC) simulations. The result is an ensemble of plausible-matches, reminiscent of model ensembles in free-form lens modelling ([Saha & Williams 2004](#); [Coles et al. 2014](#)) but having a different meaning, because they arise from galaxy-formation simulations.

The minimum of χ^2 in Eq. (12) need not correspond to a unique α . In other words, very different galaxies can in principle produce identical synthetic images. This is the well-known problem of lensing degeneracies (for a review, see [Wagner 2018](#)). The plausible matching strategy automatically marginalises over simulated galaxies that are degenerate in the observables, so lensing degeneracies as such are not an obstacle to the method. If, however, the differences between galaxy-formation scenarios happen to be aligned along lensing degeneracies, lensing observables would be ineffective as discriminators between galaxy-formation models. Such a thing seems unlikely, but we cannot rule it out at present.

In total, 11634 MCMC simulations had to be executed until the solutions for all simulated galaxies and lens systems converged. This was relatively easily achieved within about 4–8 hours per lens through some optimisations and some compromises. The inclusion of a PSF increases the non-sparseness of the synthetic-image mapping considerably, makes the generation of synthetics quite computationally intensive, and slows down the MCMC simulations by an average factor of ~ 50 . Fortunately, initial tests showed that the omission of the PSF in Eq. (9) for this step caused acceptable differences. Since both the projected surface-density maps and cutouts from the observations have been centred well beforehand, p_{rel} never deviated from the centre by more than $0.05''$, which lead us to discard that parameter in the final stage. The con-

¹ <https://github.com/spacetelescope/tinytim>

vergence to optimal alignment rotation angles on the other hand was more relevant, especially for galaxies with high ellipticity, whereas for round galaxies the rotation angles were arbitrary and usually settled around 0° .

The subsequently described lens-matching method has been implemented in the public software `gleam`² (Gravitational Lens Extended Analysis Module) by PD. It is written in Python and thus comes with all of its flexibility and a large scientific library support. Computationally demanding tasks such as the calculation of potential gradients are alternatively also implemented in a mixture of C and Cython (Behnel et al. 2011). Similar to the lens modelling tool `GLASS`³ by Coles et al. (2014), the module encompasses more general features, some of which are still in development, but the lens-matching technique lies at its core. In particular, the synthetic imager described in Subsection 2.2 is implemented in the sub-module `gleam.reconsrc`.

The entire lens-matching method was intentionally kept relatively simple and lightweight in order to keep it scalable for a much bigger lens sample using larger catalogues and to minimize the input required from the outside. Figure 2 shows a schematic graph which summarizes each key step of the lens-matching method. The analysis presented here aimed for a proof-of-concept only. With a working basis, further refinements and improvements can easily be explored in isolation and afterwards properly implemented. In Section 6, we give some suggestions of what aspects could be improved first.

3 SEAGLE

Mukherjee et al. (2018) introduced the `SEAGLE` pipeline to systematically study galaxy formation via simulated strong lenses from the EAGLE simulations (Schaye et al. 2014; Crain et al. 2015; McAlpine et al. 2016). `SEAGLE` used the `GLAMER` ray-tracing package (Gravitational Lensing with Adaptive Mesh Refinement; Metcalf & Petkova 2014; Petkova et al. 2014) to create realistic lensed images and calculate all other lensing quantities used in their analysis. `SEAGLE` aims to investigate and possibly disentangle galaxy formation and evolution mechanisms by creating, modelling, and analysing simulated strong lens-galaxies to compare them with observations.

EAGLE is a suite of state-of-the-art hydrodynamical simulations that explored several feedback scenarios and model variations giving us a set of galaxy evolution scenarios to assess their impact on the present-day universe. Crain et al. (2015) divided the simulations into two categories. The first comprises four simulations *calibrated* to yield the $z = 0.1$ galaxy stellar mass function (GSMF) and central black hole (BH) masses as a function of galaxy stellar mass. The second category comprises simulations that each vary a single sub-grid physics parameter with respect to the Reference model but without considering whether they match the GSMF (i.e. they are not calibrated).

In Mukherjee et al. (2019), using `SEAGLE`, the authors quantified that if the simulated lensed images are modelled similar to the observations, then the median total mass density slope

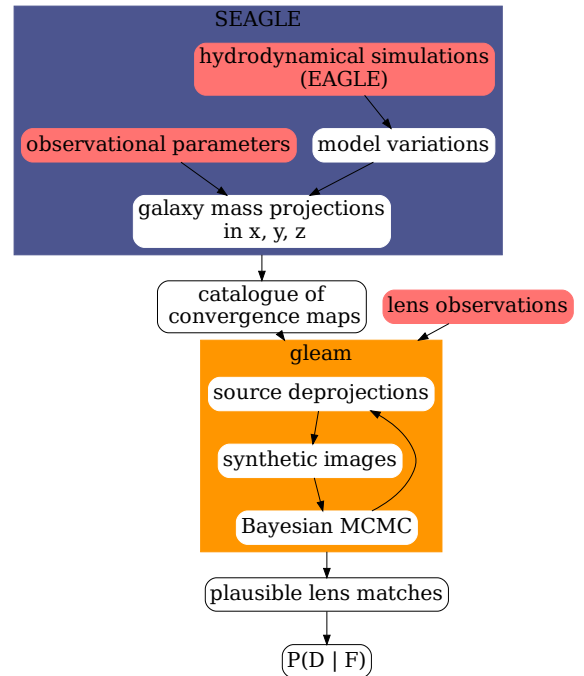


Figure 2. A schematic top-bottom graph summarizing the specific steps of the lens-matching method in this work. The pipeline was intentionally kept quite modular; in particular, the components in the blue and yellow coloured subgraphs are specific choices of this work, and could in principle be replaced by equivalent operators. Red fields represent independent data inputs from observations or simulations.

of galaxies from an inefficient AGN feedback model (AGNdT8: Reference variation) and a constant feedback model (FBconst: Calibrated simulation) that becomes inefficient at denser environment gives slopes $t=2.01$ and $t=2.07$, respectively, in good agreement with the observations of SLACS, SL2S (Strong Lensing Legacy Survey), and BELLS (Baryon Oscillation Spectroscopic Survey (BOSS) Emission-Line Lens Survey). Galaxies in the EAGLE Reference model (benchmark model), however, tend to have a steeper median total mass density slope ($t=2.24$) than observed lens galaxies (i.e. $t=2.08$ for SLACS, $t=2.11$ for BELLS and $t=2.18$ for SL2S).

The nomenclature of the `SEAGLE`-projected mass distributions in the catalogue depends on their halo, subhalo, and projection axis. A number following 'H' refers to the halo number, 'S' gives the subhalo, and letters 'A/B/G' refers to the projection the galaxy has undergone in Cartesian coordinates i.e. α , β and γ respectively. The feedback model denominations are prepended in this nomenclature.

For our analysis, we choose these two galaxy evolution scenarios (AGNdT8 and FBconst) as they are most realistic to the strong lensing observations. We briefly discuss the key features of these feedback models below.

In the calibrated simulations, the models differ in terms of their adopted efficiency of feedback associated with star formation, and how this efficiency depends upon the local environment. The general consensus shows that the properties of simulated galaxies are most sensitive to the efficiency of

² <https://github.com/phdenzel/gleam>

³ <https://github.com/jpcoles/glass>

baryonic feedback (see e.g., Schaye et al. 2010; Vogelsberger et al. 2013). Below a certain resolution limit, the physical processes cannot be simulated via the dynamics of the particles. So they are incorporated via analytic prescriptions in all hydro-dynamic simulations including EAGLE. In EAGLE model variations, the efficiency of the stellar feedback and the BH accretion were calibrated to broadly match the observed local ($z \approx 0$) GSMF. Also, several studies established that AGN feedback is a necessary ingredient for regulating the growth of massive galaxies (e.g. Crain et al. 2009; Schaye et al. 2010; Haas et al. 2013).

Below we briefly describe the EAGLE galaxy formation models which were used in this work.

3.1 A Constant Feedback (FBconst)

The simplest feedback model used in EAGLE is FBconst. In this calibrated model, independently from the local conditions, a fixed amount of energy per unit stellar mass is injected into the ISM. This fixed energy corresponds to the total energy discharged by type-II SNe ($f_{\text{th}} = 1$). While the stellar feedback in this model was not calibrated, the model does reproduce the observables used for the calibration. Crain et al. (2015) found that the thermal stellar feedback prescription employed in EAGLE becomes inefficient at high gas densities due to resolution effects (Vecchia & Schaye 2012). Thus in this model, there is a lack of compensation for more energy at higher gas density. Thus the stellar feedback will be less effective in high-mass galaxies (where the gas tends to have higher densities) (Crain et al. 2015).

Schaye et al. (2014) demonstrated that it is possible to calibrate the Reference model to reproduce the GSMF and the observed sizes (in different bands) of galaxies at $z = 0.1$. Crain et al. (2015) conducted a series of simulations (listed in the lower section of Table 1 therein) for which the value of a single parameter was varied from that adopted in the Reference model. One of the parameters varied was AGN temperature.

3.2 Temperature variation in AGN heating (AGNdT8)

Schaye et al. (2014) have examined the role of the AGN heating temperature in EAGLE by adopting $\Delta T_{\text{AGN}} = 10^{8.5}\text{K}$ and 10^9K . They demonstrated that a higher heating temperature produces less frequent but more energetic AGN feedback episodes. They concluded it is necessary to reproduce the gas fractions and X-ray luminosities of galaxy groups. Brun et al. (2014) also concluded that higher heating temperature yields more efficient AGN feedback. There are two Reference-model variation simulations with $\Delta T_{\text{AGN}} = 10^8\text{K}$ (AGNdT8) and $\Delta T_{\text{AGN}} = 10^9\text{K}$ (AGNdT9), besides the Reference model itself which adopted $\Delta T_{\text{AGN}} = 10^{8.5}\text{K}$. In massive galaxies, the heating events (less frequent but more energetic) are more effective at regulating star formation due to a higher heating temperature. AGNdT8 (AGNdT9) model has a higher (lower) peak star fraction compared to the Reference model. The reduced efficiency of AGN feedback, when a lower heating temperature is adopted, leads to the formation of more compact galaxies because gas can more easily accrete onto the centers of galaxies and form stars. Mukherjee et al.

(2018) showed that for galaxy-galaxy strong lenses, AGNdT8 produces closest analogs for SLACS. Thus, for this work, we use galaxies from the AGNdT8 simulation, in addition to the galaxies from the simpler FBconst model.

4 THE OBSERVED SYSTEMS

In order to test whether searching for plausible matches from EAGLE simulations is at all feasible, we selected a small sample of seven lens systems that have already been studied by other methods. The selection was based on three criteria. First, the system had to be clearly strongly lensed, with relatively easily identifiable images showing very clear evidence of multiple imaging. Second, the observations needed to have extended images and arcs with some imperfections (rather than point-like lensed quasars) so as to challenge the matching technique. Third, the sample had to be representative of a larger sample of lenses. The third criterion made it natural to choose from SLACS, and from the SLACS lenses of quality category ‘‘A’’ we selected seven, having a wide range of mean image radii, which is a rough proxy for Einstein radii. Figs. 4–10 in their top left panels show the lensed images in HST-image F814W bands. The most relevant information about the systems is listed in Table 1, including references to the discovery papers.

4.1 SDSSJ0029–0055

SDSSJ0029–0055 appears to be a relatively small, doubly lensing system observed on 12 September 2006. Initial reports by Bolton et al. (2008) classify it as a single, early-type galaxy. The redshift of the foreground galaxy was spectroscopically measured to $z_L = 0.2270$ and for the background source to $z_S = 0.9313$. It exhibits an almost fully closed ring which is relatively difficult to recognize due to the light pollution from the foreground galaxy. A de Vaucouleurs fit to the lensing galaxy gives a relatively high effective radius of $2.16''$. It also has a well measured stellar velocity dispersion of $\sigma_{\text{SDSS}} = 229 \pm 18 \text{ km s}^{-1}$.

The initial report presented a singular isothermal ellipsoid and light-traces-mass gravitational lens model which provided best fits using two source-plane components. However, the present work indicates that a single-component source (see second image in the left column in Figure 4) is also possible. The top image in Figure 4 in the left column shows the system from the HST/ACS-WFC1 observation (Advanced Camera System Wide Field Channel 1) using the F814W filter.

4.2 SDSSJ0737+3216

SDSSJ0737+3216 appeared in the first SLACS report by Bolton et al. (2006). A successive report (Bolton et al. 2008) grades the quality of the single-multiplicity, early-type galaxy to be of type ‘‘A’’. Its foreground and background redshifts were measured to $z_L = 0.3223$ and $z_S = 0.5812$ respectively. From SDSS spectroscopic data, a good estimate for the velocity dispersion of $\sigma_{\text{SDSS}} = 338 \pm 17 \text{ km s}^{-1}$ was provided.

Parametric lens models from Bolton et al. (2008) used two source-plane components to fit the astrometric data. The

Name	R.A. [hms]	Decl. [dms]	z_l	z_s	σ_{SDSS} [km/s]	R_{eff} [arcsec]	Reference
SDSSJ0029−0055	00:29:07.8	−00:55:50	0.23	0.93	229 ± 18	2.16	(1)
SDSSJ0737+3216	07:37:28.5	+32:16:18	0.32	0.58	310 ± 15	2.16	(2)
SDSSJ0753+3416	07:53:46.2	+34:16:33	0.14	0.96	208 ± 12	1.89	(3)
SDSSJ0956+5100	09:56:29.8	+51:00:06	0.24	0.47	299 ± 16	2.33	(2)
SDSSJ1051+4439	10:51:09.4	+44:39:08	0.16	0.54	216 ± 16	1.66	(3)
SDSSJ1430+6104	14:30:34.8	+61:04:04	0.17	0.65	180 ± 15	2.24	(3)
SDSSJ1627−0053	16:27:46.5	−00:53:57	0.21	0.52	275 ± 12	2.08	(2)

Table 1. Summary of the observed lensing systems. (1) Bolton et al. (2008); (2) Bolton et al. (2006); (3) Shu et al. (2017)

HST/ACS-WFC1 observation (on 21 September 2004) using the F814W filter is displayed in the top image in the left column of Figure 5. It shows two extended images of which the brighter image is most likely the product of two merged ones, and a point-like image connected via a dim arc, which would most likely classify it as a short-axis quad. Besides the initial modelling, Ferreras et al. (2007) provided a free-form lens model for this lens system, along with a spatially resolved comparison to the stellar-mass surface distribution derived from population-synthesis models.

4.3 SDSSJ0753+3416

The top image of the left column in Figure 6 shows SDSSJ0753+3416 (HST/ACS WFC1 F814W on 8 September 2010) as a clearly lensing system. It is a very interesting system with minimum eight (possibly even 12) lensed images of at least two sources. Shu et al. (2017) reports ellipsoid lens models using even four source-plane components. Either way, this lens promises a much lower degree of degeneracy due to the high number of lensed images and sources.

From the SDSS observations the lensing galaxy was classified as an early-type, single-multiplicity foreground galaxy with a well measured velocity dispersion $\sigma_{\text{SDSS}} = 206 \pm 11 \text{ km s}^{-1}$. The redshift estimates for the lens and source are $z_L = 0.1371$ and $z_S = 0.9628$, respectively.

4.4 SDSSJ0956+5100

In the left column of Figure 7, the top image shows SDSSJ0956+5100 from the HST/ACS-WFC1 F814W observation from 1 November 2006. Bolton et al. (2006) designates its lens an early-type, single foreground galaxy. The spectroscopic survey yielded a velocity dispersion of $\sigma_{\text{SDSS}} = 299 \pm 16 \text{ km s}^{-1}$ and redshifts of $z_L = 0.2405$ and $z_S = 0.4700$ for the foreground and background source respectively.

The lens shows four lensed source images at various angular separations from the lensing galaxy in a short-axis quad configuration. Two of the images appear rather point-like and bright whereas the others are extended and fainter.

It is another lens which was free-form modelled by Ferreras et al. (2007). The models predict it to be a rather high-mass galaxy with a total and stellar mass within the aperture image radius R_M of

$$M_{\text{tot}}(< R_M) = 66.4_{-16.7}^{+25.7} \cdot 10^{10} M_{\odot} \text{ and}$$

$$M_{\text{star}}(< R_M) = 41.8_{-4.0}^{+4.9} \cdot 10^{10} M_{\odot},$$

where the aperture radius is $2R_{\text{max}} - R_{\text{min}}$, the difference

of projected radii of twice the outermost and innermost lens images.

4.5 SDSSJ1051+4439

Shu et al. (2017) reports SDSSJ1051+4439 as another early-type, single foreground-galaxy lens system. The SDSS data yields a velocity dispersion value of $\sigma_{\text{SDSS}} = 216 \pm 16 \text{ km s}^{-1}$; the redshifts of the lens and background source are reported with $z_L = 0.1634$ and $z_S = 0.5380$ respectively. While the image shown in Figure 8 (left column, top panel) does not clearly indicate that the supposedly doubly lensing system is indeed lensing, its type is still classified as “A”.

4.6 SDSSJ1430+6104

Figure 9 (first image in the left column) depicts SDSSJ1430+6104 (HST/ACS-WFC1 F813W) as a very noisy lens system with faint lensed images, with considerable pollution by the host galaxy. Shu et al. (2017) reports the early-type galaxy with a velocity dispersion value of $\sigma_{\text{SDSS}} = 180 \pm 15 \text{ km s}^{-1}$. The SDSS redshifts for the foreground and background objects are $z_L = 0.1688$ and $z_S = 0.6537$.

The parametric, ellipsoid lens models use two source-plane components to fit the photometric data, with a total mass within the Einstein radius of $1.02 \cdot 10^{11} M_{\odot}$.

4.7 SDSSJ1627−0053

On 12 March 2006, the HST/ACS-WFC1 observed SDSSJ1627−0053 as a double with an almost completely closed ring. Bolton et al. (2006) reported it as an early-type foreground galaxy in a single-multiplicity system with redshifts $z_L = 0.2076$ and $z_S = 0.5241$. The spectroscopically determined velocity dispersion is well measured with a value of $\sigma_{\text{SDSS}} = 290 \pm 15 \text{ km s}^{-1}$. A picture of the lens system can be found on the top panel of the left column in Figure 10.

5 RESULTS

The results on plausible matches for the seven lens systems considered are displayed in Figs. 4–10 and summarised in Table 2. Figs. 4–10 are devoted to one lens each, in the same order as in Table 1.

Each of these figures has eight panels, arranged as follows.

Observed image	Synthetic image
Source brightness	Residual Image
Lensing mass	Pixelized lensing mass
Lensing Roche potential	Mean enclosed convergence

We now discuss properties of the most-plausible matches as shown in Figs. 4–10.

5.1 Images

The top row of Figs. 4–10 shows the observed lensed images and the synthetic image from the most-plausible match. The lensing galaxy is masked out. The difference between these, scaled by the noise — in other words, the pixelwise χ^2 from Eq. (12) — is shown in the right panel of the second row.

For the MCMC over the orientation ϕ_{rel} it is computationally simpler to rotate the image rather than the lens. As a result, there are some rotated-corner artifacts, less noticeable in the synthetic images, but at the edges of the source plane, especially for example in Figure 8. These are, however, harmless χ^2 computation, for which only a circular region was considered.

In all of the second-row right panels, it is evident that the contributions to χ^2 come mainly from an annular region where the multiply-imaged features are. The black inner disc is of course just the masked-out lensing galaxy. The outer part in the χ maps is dark (or at a lower level) because without multiple images the source brightness has the trivial solution

$$s(\boldsymbol{\theta} - \boldsymbol{\alpha}(\boldsymbol{\theta})) = I^{\text{obs}}(\boldsymbol{\theta}) \quad (13)$$

and then any contribution to χ^2 comes only because there are fewer pixels in the source plane than in the image plane. It would be better to consider only the multiply-imaged region when computing χ^2 , but it is not clear how to do so efficiently.

5.2 Source reconstructions

The left panel in the second row in each of Figs. 4–10 shows the reconstructed $s(\boldsymbol{\beta})$ for the most-plausible match. The sources appear fragmented on small scales because of a discretisation artefact explained in Subsection 2.2 which we have not interpolated out.

The source-fitting as implemented here does not guarantee that the reconstructed source will be blob-like and not a random scatter plot. However, plausible matching lenses are generally associated with plausible looking source maps (disregarding the small-scale fragmentation). In cases where the data are more noisy the source plane also tends to be noisy; this is especially noticeable in J0737+3216, J1051+4439, and J1430+6104 (Figures 5, 8, and 9), where the bright specks from the data images (probably artifacts left by cosmic particles) also appear in the source plane. While most sources seem to be rather symmetric, J0753+3416 (Figure 6) and J0956+5100 (Figure 7) appear to be amorphous with multiple cores. This could be an indication of a merging system or multi-component source, however further investigation is needed to confirm this.

A curious artifact appears in the cases of J0956+5100 (Figure 7) and J1051+4439 (Figure 8). There the source appears to have bright edges in a curved diamond shape. The curved edges evidently correspond to the diamond caustic for

four-image lenses, which correspond extreme magnification, and single pixels along these edges can map to large areas on the image plane. We conjecture that the source-fitting procedure is using this property of caustics to fit noise in the images.

In comparison with source reconstructions from previous works, some differences are noticeable. In most cases, general shapes of the sources agree with previous works, when noise is ignored, especially for J0029–0055. For J0753+3416 and J1430+6104 the main cores exhibit similar shapes, but previous works include more secondary sources compared to most source reconstructions here. Contrarily, J0956+5100, although being very noisy, seems to exhibit more components than reconstructions from previous works.

5.3 Mass maps

The third row in each of Figs. 4–10 shows the κ maps from SEAGLE and the reduced-resolution κ_n maps that we actually used, for the most-plausible match. The dark contours indicate $\kappa = 1$.

Interestingly, while the catalogue did include many projected surface-densities with high ellipticity, the lens-matching approach seems to preferentially select rather round models. However, this of course depends on the selection of the lens system and considering to the light profiles of the lenses in the data, mass distributions with low ellipticity were to be expected. The mass models do, however, exhibit a moderate amount of substructure.

The bottom-right panel in each of Figs. 4–10 shows the mean enclosed density $\langle \kappa \rangle_\theta$ within a given angular radius for the 10 most plausible matches in the sense of χ^2 . As in Figure 1 $\langle \kappa \rangle_\theta = 1$ is understood as the Einstein radius. The value is well-constrained, even if we consider the 50 most-plausible matches as illustrated, or in a subset of best-matching models with $\chi^2_\nu < 5$ as in Table 2.

5.4 Lensing Roche potentials

The bottom-left panels in Figs. 4–10 show another interesting quantity, a contour map of the *lensing Roche potential*

$$\mathcal{P}(\boldsymbol{\theta}) = \frac{1}{2}\theta^2 - \psi(\boldsymbol{\theta}) \quad (14)$$

which we introduced in Denzel et al. (2020b). The lens equation (8) is equivalent to

$$\boldsymbol{\beta} = \nabla \mathcal{P}(\boldsymbol{\theta}) \quad (15)$$

and consequently the points where $\nabla \mathcal{P} = 0$ are image locations from a source at $\boldsymbol{\beta} = 0$. These points are extrema (minima, maxima, and saddle-points) of $\nabla \mathcal{P}$ and easy to discern on a contour map. The actual image positions will be somewhat different, depending on the details of $s(\boldsymbol{\beta})$, but nevertheless, the contours of the lensing Roche potential offer a simple confirmation that a plausible match is indeed a strongly lensing system, and that we have not simply stumbled upon the trivial solution (13).

5.5 Relative posteriors

Every pre-selected model was match-tested against the observational data of each lens according to Eq. (12), which

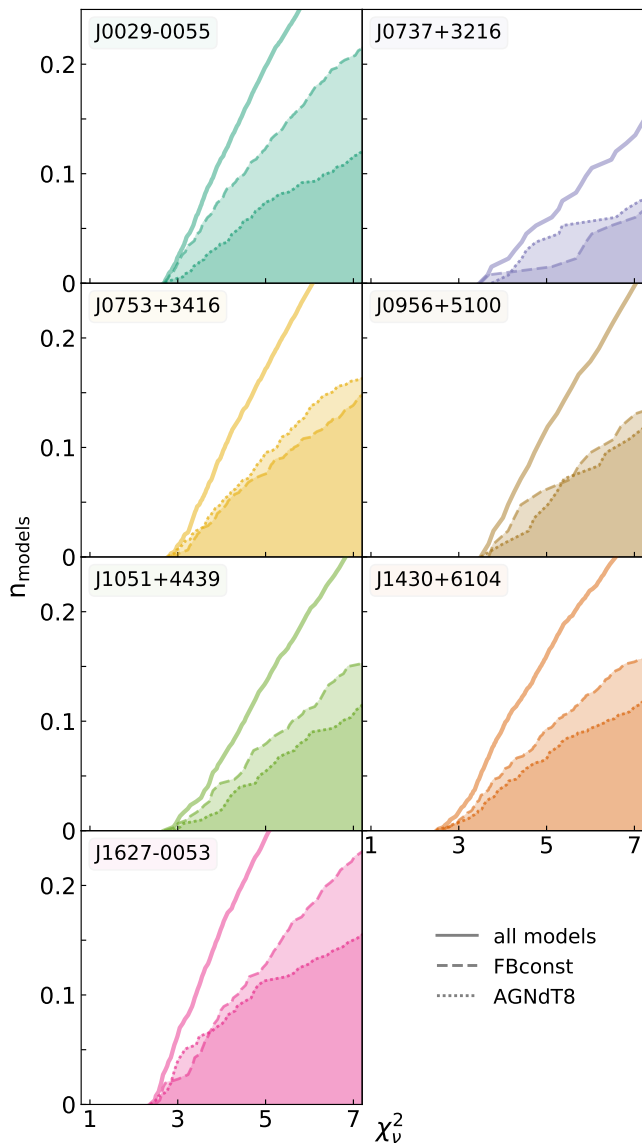


Figure 3. Cumulative χ^2_ν histograms for all match-tested models. The dotted lines show the fractions of models with feedback scheme AGNdT8, whereas the dashed lines are for FBconst models. The numbers of models n_{models} were normalized by the total numbers of models, preselected for each lens individually. Models with high χ^2_ν are considered bad matches to the observations. For instance, for the lens systems J0737+3216 and J0956+5100 only a few plausible matches have been found within the model catalogue.

yielded distributions of reduced least squares χ^2_ν . Figure 3 shows these distributions as cumulative histograms, including the fractions of models from the two galaxy-formation scenarios, FBconst and AGNdT8.

Subsets of most-plausible matches, that is, matches with minimal χ^2_ν , are likely to contain models from both galaxy-formation scenarios, evident in Table 2 and Figure 3.

Considering the most-plausible matches with e.g. $\chi^2_\nu < 5$, we can evaluate a Bayesian evidence in the form

$$\frac{P(\text{AGNdT8} | D)}{P(\text{FBconst} | D)}$$

for each lens. Using the values from Table 2, this is between

0.6 and 0.7 for J0029–0055, J0956+5100, J1051+4439, and J1430+6104, meaning these systems show a slight tendency towards FBconst. For J0737+3216 and J0753+3416 the expression above evaluates to well above 1.0, indicating a tendency towards AGNdT8, whereas for J1627–0053 it is very close to 1.0. Although, it should be noted that these values are not significant yet (especially for J0737+3216 and J0956+5100) and for better statistics more matching tests should be performed. With more match-tests and better statistics, the criterion $\chi^2_\nu < 5$ can be lowered to ensure that only the best-matching models are used to evaluate the relative posterior probability distribution. This threshold depends on the individual systems and galaxy models used in the matching method. In this case, models with χ^2_ν above 5 start to display various noticeable deficits in the source reconstructions and synthetic images and are therefore not suitable to estimate the relative posterior.

Table 2 also lists the subsets’ median values of the Einstein radii which is a measurement of the total mass the lens. These values are consistent with previous studies (Bolton et al. 2008, 2006; Shu et al. 2017; Ferreras et al. 2007). The comparison of the median stellar masses of the model galaxies with previous estimates also seem to agree well, if it is considered that previous estimates are within an Einstein radius or half-light radius of the lensing galaxies, whereas for our models it is possible to estimate the entire mass in stars.

6 DISCUSSION

Mass reconstructions in gravitational lensing are in general non-unique. Even for strong-lensing clusters with tens of multiply-imaged systems over a range of redshifts, there is significant scatter among mass models even if they fit the data equally well (see e.g., Meneghetti et al. 2017). For galaxy lenses the non-uniqueness of models is much more evident, and indeed has been known since the earliest days of lens modelling (Young et al. 1981). This facts suggests that the large catalogues of simulated galaxies in recent galaxy-formation simulations may contain plausible matches to individual observed lensing galaxies. In this work we search for and find plausible matches among EAGLE simulated galaxies to seven observed lensing galaxies from SLACS. The main computational part is to fit for (a) an orientation of a given simulated galaxy and (b) a source light distribution, such that the observed light distribution is reproduced. This is implemented in the new `gleam` code, but automated lens-modelling tools such as `AutoLens` (Nightingale et al. 2018) and `Ensai` (Hezaveh et al. 2017) could probably also be adapted for the purpose, if required.

The main conclusion of this work is that EAGLE — and presumably other comparable galaxy-formation simulations — contain plausible matches for observed lensing galaxies. Hence it appears feasible to use observed lensing galaxies as constraints on galaxy-formation scenarios, without conventional lens models. Obtaining statistically significant results, however, will need several issues to be addressed first, which we discuss briefly below.

- (i) In this work we have used single simulated galaxies, disregarding the environment and line-of-sight structures, and also approximated the projected mass as consisting of 23×23 mass tiles. Furthermore, we have considered rotations only

Lens	$N_{\chi^2_{\nu} < 5}$	$N_{\chi^2_{\nu} < 5}$	χ^2_{ν}	χ^2_{ν}	$\delta\phi_{\text{rel}}$	θ_{E}	M_{stel}
	AGNdT8	FBconst	AGNdT8	FBconst	[$^{\circ}$]	[$''$]	[$10^{11} M_{\odot}$]
SDSSJ0029–0055	52	86	2.71	2.68	$11.1^{+3.3}_{-3.3}$	$1.04^{+0.08}_{-0.08}$	$1.30^{+0.20}_{-0.22}$
SDSSJ0737+3216	6	2	3.74	3.47	$4.8^{+0.7}_{-0.7}$	$1.09^{+0.01}_{-0.03}$	$3.84^{+1.56}_{-0.88}$
SDSSJ0753+3416	61	48	2.78	2.84	$15.8^{+3.1}_{-3.1}$	$1.39^{+0.11}_{-0.09}$	$1.67^{+0.21}_{-0.53}$
SDSSJ0956+5100	4	6	3.50	3.68	$3.7^{+1.0}_{-1.0}$	$1.48^{+0.16}_{-0.03}$	$5.85^{+1.17}_{-0.19}$
SDSSJ1051+4439	17	24	2.90	2.69	$9.4^{+2.1}_{-2.1}$	$1.56^{+0.16}_{-0.09}$	$3.53^{+0.66}_{-0.40}$
SDSSJ1430+6104	41	58	2.49	2.65	$5.1^{+1.2}_{-1.2}$	$1.22^{+0.07}_{-0.11}$	$1.84^{+0.20}_{-0.35}$
SDSSJ1627–0053	30	33	2.37	2.48	$17.5^{+5.5}_{-5.5}$	$1.40^{+0.12}_{-0.08}$	$3.52^{+0.33}_{-0.50}$

Table 2. Results for a subset of the most plausible matches for each lens system with $\chi^2_{\nu} < 5$. The reduced χ^2_{ν} apply to the best synthetic images of the matching tests, $\delta\phi_{\text{rel}}$ are the average deviations in orientations about the line of sight of the 68% interval from the MCMC of all models in the subset. The θ_{E} column contains medians of Einstein radii and the M_{stel} column medians of the total mass in stars of the simulated galaxy models, with uncertainties covering the 68% interval of the model subset.

about three orthogonal candidate lines of sight, rather than arbitrary orientations in 3D. All these aspects of the implementation need to be improved, while keeping it efficient for the purpose of scaling up to larger lens samples.

- (ii) The source reconstruction is another area that can be improved. The advantage of the procedure used in this work is that supervision at the level of individual lenses is not required, though this will not be true if the observation data is dominated by noise and extraneous light, because additional masks would be needed. The disadvantage of the current procedure is that the fitted source is just an arbitrary brightness map, and the principle of plausible matches is not being applied.
- (iii) Since plausible-matching galaxies for any given lens always have very similar Einstein radii, even though they may differ in other ways, it is advantageous to pre-select the simulated galaxies to be within a suitable range of Einstein radii. In this work, we produced a conventional lens model first, but a more efficient method is desirable.
- (iv) Provided the lensing galaxy is clearly visible in the data, stellar mass estimated from multi-band images using population synthesis (cf. Leier et al. 2016) could be incorporated into the likelihood $P(D|g)$. Stellar-maps from the simulations are, of course, known a priori. Ideally, the stellar light distribution would be subtracted from the entire observational data using models of the galaxy light.
- (v) Stellar kinematics would be an important ingredient in $P(D|g)$. Current simulations soften the gravitational dynamics on scales of order a kpc (see e.g., Table 2 in Schaye et al. 2014), and it would be interesting to see if this strongly affects $P(D|g)$. It would also be interesting to see if an equilibrium galaxy-modelling framework like AGAMA, which resolves much smaller scales, yields higher $P(D|g)$ than cosmological simulation.
- (vi) Finally, although available for only a small fraction of lenses, time time-delays (for recent observations see ?) would be interesting to incorporate in the plausible-match scheme. Lensing time delays are usually thought of as a way of measuring cosmological parameters, especially H_0 . But the accuracy of the H_0 inferences from lensing depends on how well $P(g|F)$ of the universe is constrained. Hence time delays could be useful (if they turn out to be not the best way to measure H_0) with cosmological parameter-values taken from other methods, as a way of constraining $P(g|F)$.

ACKNOWLEDGMENTS

We would like to thank Liliya L. R. Williams for useful discussions and comments on the paper.

We also thank the anonymous referee for the constructive suggestions to bring the paper to its final form.

PD acknowledges support from the Swiss National Science Foundation. SM acknowledges the funding from the European Research Council (ERC) under the EUs Horizon 2020 research and innovation programme (COSMICLENs; grant agreement no. 787886).

This research is based on observations made with the NASA/ESA Hubble Space Telescope obtained from the Space Telescope Science Institute, which is operated by the Association of Universities for Research in Astronomy, Inc., under NASA contract NAS 5–26555. These observations are associated with programs #10886, #10174, #12210, #10494.

DATA AVAILABILITY

The data underlying this article are available at the STScI (<https://mast.stsci.edu/>; the unique identifiers are cited in the acknowledgements). The derived data generated in this research will be shared on request to the corresponding author, or can be replicated using the open-source software available at:  <https://github.com/phdenzel/gleam>.

REFERENCES

- AbdelSalam H. M., Saha P., Williams L. L. R., 1998, *Monthly Notices of the Royal Astronomical Society*, 294, 734
- Barnabè M., Nipoti C., Koopmans L. V. E., Vegetti S., Ciotti L., 2009, *Monthly Notices of the Royal Astronomical Society*, 393, 1114
- Behnel S., Bradshaw R., Citro C., Dalcin L., Seljebotn D. S., Smith K., 2011, *Computing in Science & Engineering*, 13, 31
- Bolton A. S., Burles S., Koopmans L. V. E., Treu T., Moustakas L. A., 2006, *The Astrophysical Journal*, 638, 703
- Bolton A. S., Burles S., Koopmans L. V. E., Treu T., Gavazzi R., Moustakas L. A., Wayth R., Schlegel D. J., 2008, *The Astrophysical Journal*, 682, 964
- Brun A. M. C. L., McCarthy I. G., Schaye J., Ponman T. J., 2014, *Monthly Notices of the Royal Astronomical Society*, 441, 1270
- Coles J. P., Read J. I., Saha P., 2014, *Monthly Notices of the Royal Astronomical Society*, 445, 2181

- Collett T. E., 2015, *Astrophysical Journal*, 811, 20
- Crain R. A., et al., 2009, *Monthly Notices of the Royal Astronomical Society*, 399, 1773
- Crain R. A., et al., 2015, *Monthly Notices of the Royal Astronomical Society*, 450, 1937
- Davies A., Serjeant S., Bromley J. M., 2019, *Monthly Notices of the Royal Astronomical Society*, 487, 5263
- Denzel P., Coles J. P., Saha P., Williams L. L. R., 2020a, arXiv e-prints, p. [arXiv:2007.14398](https://arxiv.org/abs/2007.14398)
- Denzel P., Mukherjee S., Coles J. P., Saha P., 2020b, *Monthly Notices of the Royal Astronomical Society*, 492, 3885–3903
- Ding X., et al., 2020, arXiv e-prints, p. [arXiv:2006.08619](https://arxiv.org/abs/2006.08619)
- Ferreras I., Saha P., Burles S., 2007, *Monthly Notices of the Royal Astronomical Society*, 383, 857
- Gomer M. R., Williams L. L. R., 2017, *Monthly Notices of the Royal Astronomical Society*, 475, 1987
- Haas M. R., Schaye J., Booth C. M., Vecchia C. D., Springel V., Theuns T., Wiersma R. P. C., 2013, *Monthly Notices of the Royal Astronomical Society*, 435, 2955
- Hezaveh Y. D., Levasseur L. P., Marshall P. J., 2017, *Nature*, 548, 555
- Hopkins P. F., Kereš D., Oñorbe J., Faucher-Giguère C.-A., Quataert E., Murray N., Bullock J. S., 2014, *Monthly Notices of the Royal Astronomical Society*, 445, 581
- Krist J. E., Hook R. N., Stoehr F., 2011. SPIE, doi:10.1117/12.892762, <https://doi.org/10.1117/12.892762>
- Küing R., et al., 2018, *Monthly Notices of the Royal Astronomical Society*, 474, 3700
- Leier D., Ferreras I., Saha P., Charlot S., Bruzual G., La Barbera F., 2016, *Monthly Notices of the Royal Astronomical Society*, 459, 3677
- Marshall P. J., et al., 2016, *Monthly Notices of the Royal Astronomical Society*, 455, 1171
- McAlpine S., et al., 2016, *Astronomy and Computing*, 15, 72
- Meneghetti M., et al., 2017, *Monthly Notices of the Royal Astronomical Society*, 472, 3177
- Metcalf R. B., Petkova M., 2014, *Monthly Notices of the Royal Astronomical Society*, 445, 1942
- Millon M., et al., 2020, COSMOGRAIL XIX: Time delays in 18 strongly lensed quasars from 15 years of optical monitoring ([arXiv:2002.05736](https://arxiv.org/abs/2002.05736))
- Mukherjee S., et al., 2018, *Monthly Notices of the Royal Astronomical Society*, 479, 4108
- Mukherjee S., Koopmans L. V. E., Metcalf R. B., Tortora C., Schaller M., Schaye J., Vernardos G., Bellagamba F., 2019, arXiv e-prints,
- Nightingale J. W., Dye S., Massey R. J., 2018, *Monthly Notices of the Royal Astronomical Society*, 478, 4738
- Petkova M., Metcalf R. B., Giocoli C., 2014, *Monthly Notices of the Royal Astronomical Society*, 445, 1954
- Saha P., Williams L. L. R., 2004, *Astronomical Journal*, 127, 2604
- Saha P., Coles J., Macciò A. V., Williams L. L. R., 2006, *The Astrophysical Journal*, 650, L17
- Schaye J., et al., 2010, *Monthly Notices of the Royal Astronomical Society*, 402, 1536
- Schaye J., et al., 2014, *Monthly Notices of the Royal Astronomical Society*, 446, 521
- Shu Y., et al., 2017, *The Astrophysical Journal*, 851, 48
- Vasiliev E., 2018, *Monthly Notices of the Royal Astronomical Society*, 482, 1525
- Vecchia C. D., Schaye J., 2012, *Monthly Notices of the Royal Astronomical Society*, 426, 140
- Vogelsberger M., Genel S., Sijacki D., Torrey P., Springel V., Hernquist L., 2013, *Monthly Notices of the Royal Astronomical Society*, 436, 3031
- Vogelsberger M., et al., 2014, *Monthly Notices of the Royal Astronomical Society*, 444, 1518
- Wagner J., 2018, *Astronomy & Astrophysics*, 620, A86
- Wagner J., Liesenborgs J., Eichler D., 2019, *Astronomy & Astrophysics*, 621, A91
- Walsh D., Carswell R. F., Weymann R. J., 1979, *Nature*, 279, 381
- Yildirim A., Suyu S. H., Halkola A., 2020, *Monthly Notices of the Royal Astronomical Society*, 493, 4783
- Young P., Gunn J. E., Oke J. B., Westphal J. A., Kristian J., 1980, *The Astrophysical Journal*, 241, 507
- Young P., Gunn J. E., Oke J. B., Westphal J. A., Kristian J., 1981, *The Astrophysical Journal*, 244, 736

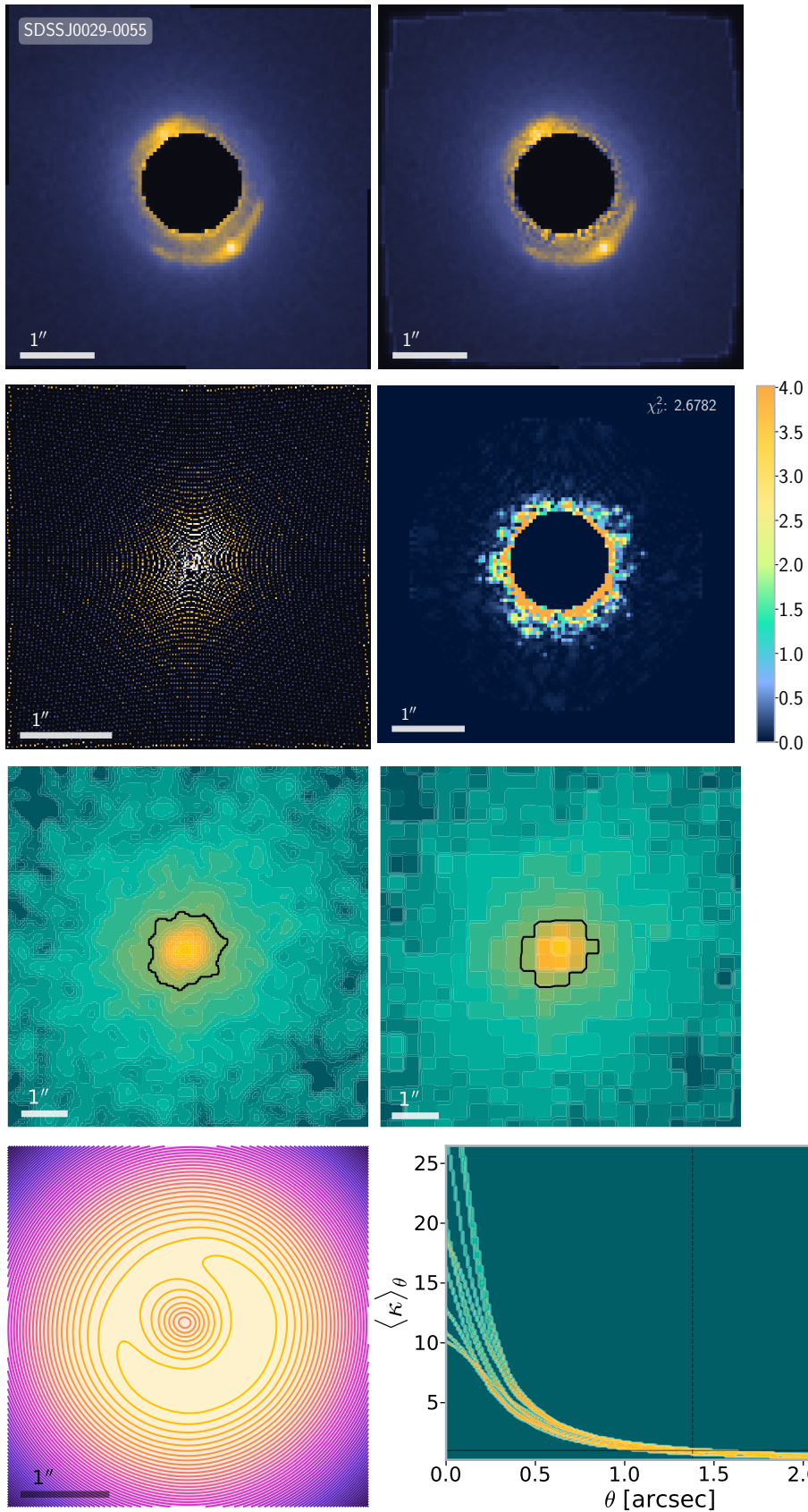


Figure 4. Results for SDSS J0029-0055. See Section 5 for details.

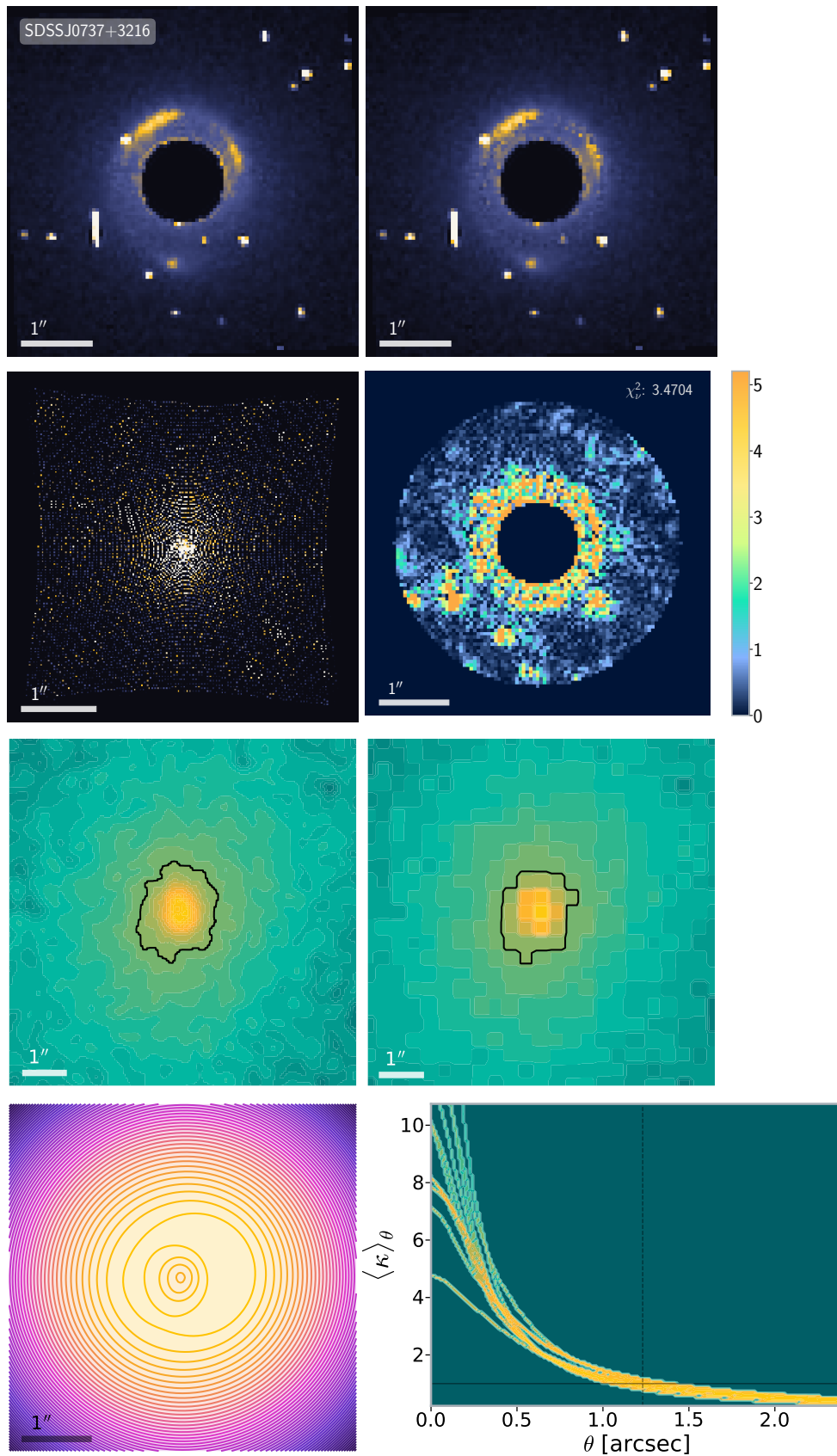


Figure 5. Results for SDSS J0737+3216. See Section 5 for details.

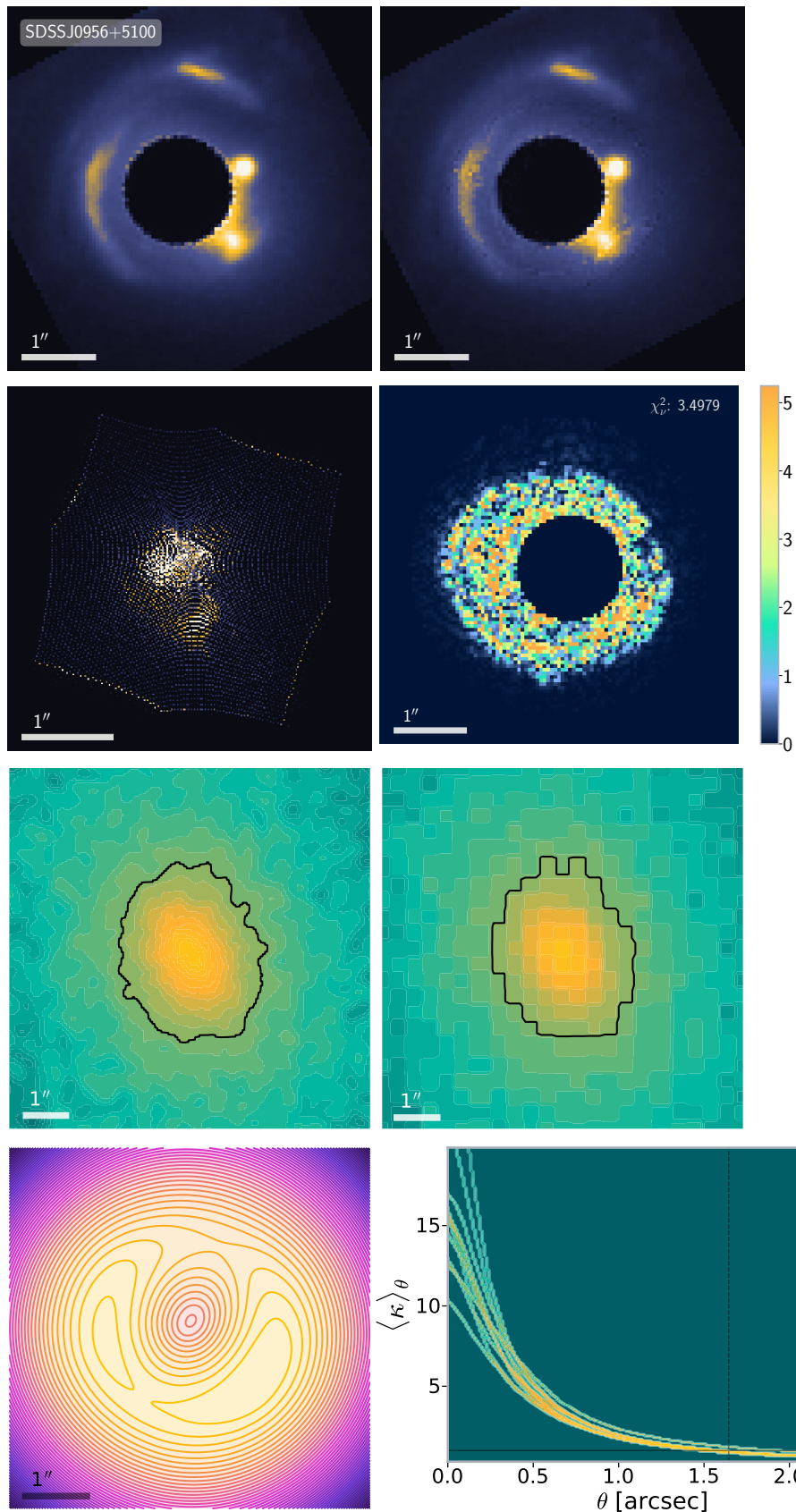


Figure 7. Results for SDSS J0956+5100. See Section 5 for details.

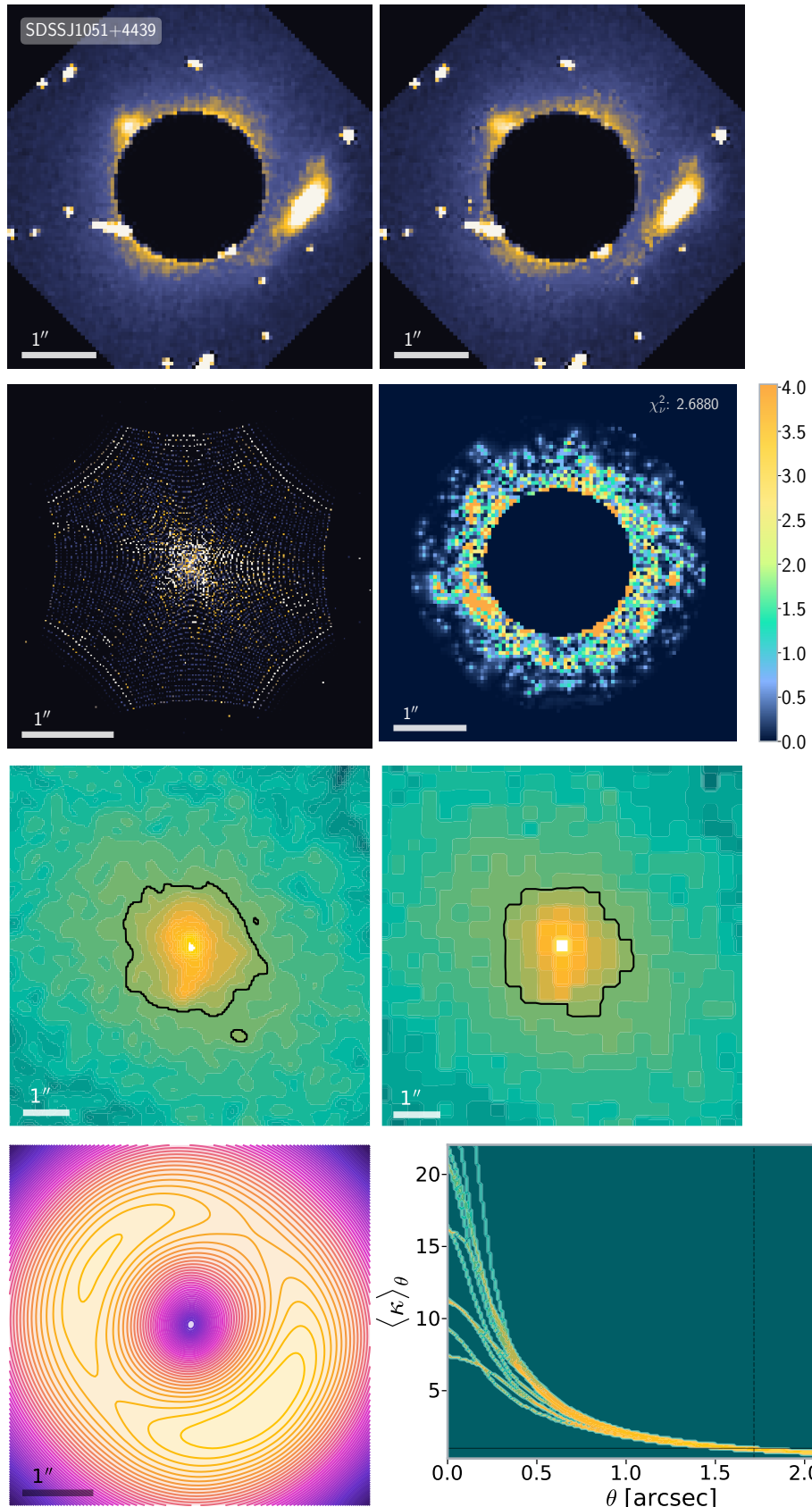


Figure 8. Results for SDSS J1051+4439. See Section 5 for details.

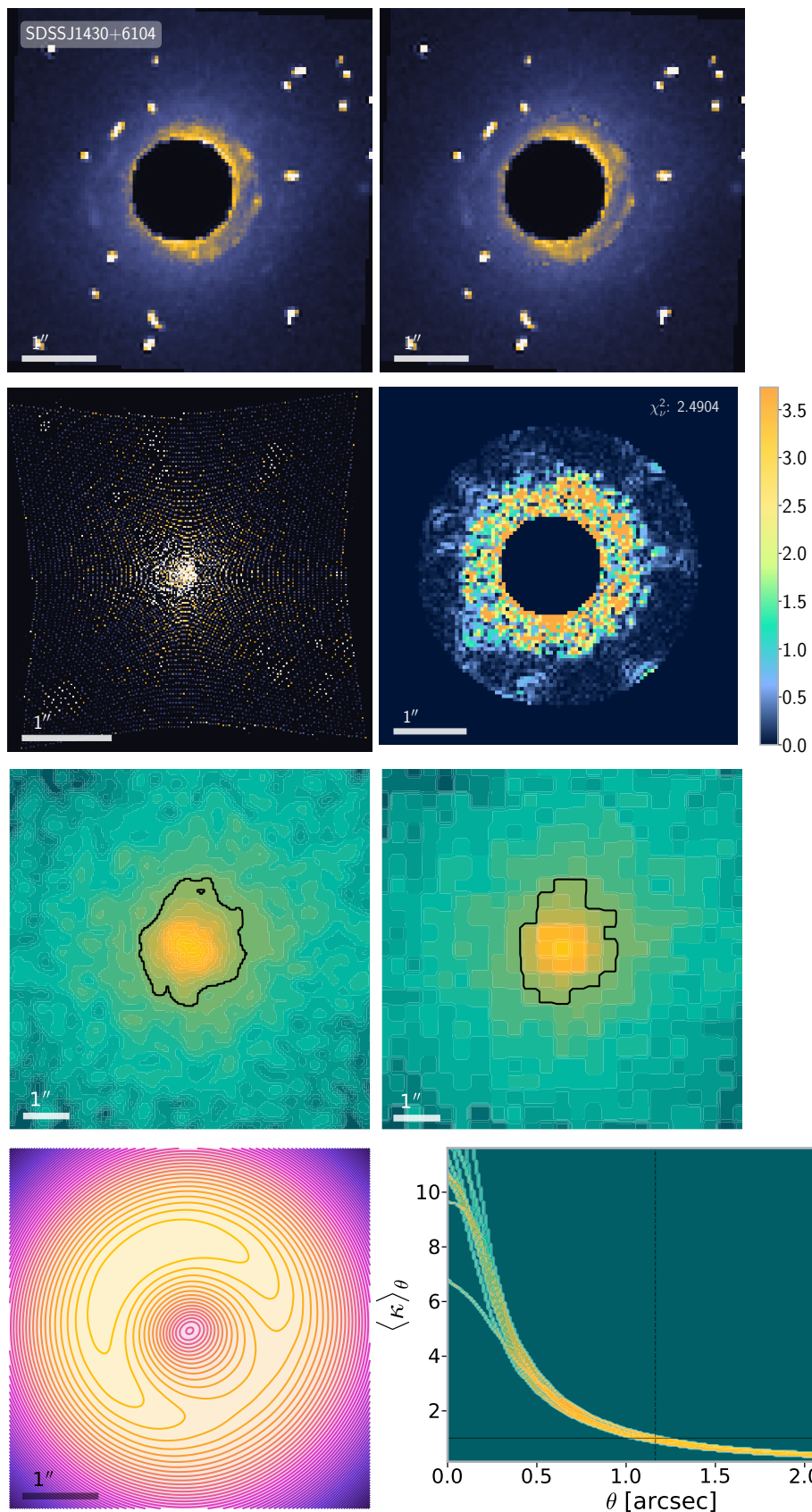


Figure 9. Results for SDSS J1430+6104. See Section 5 for details.

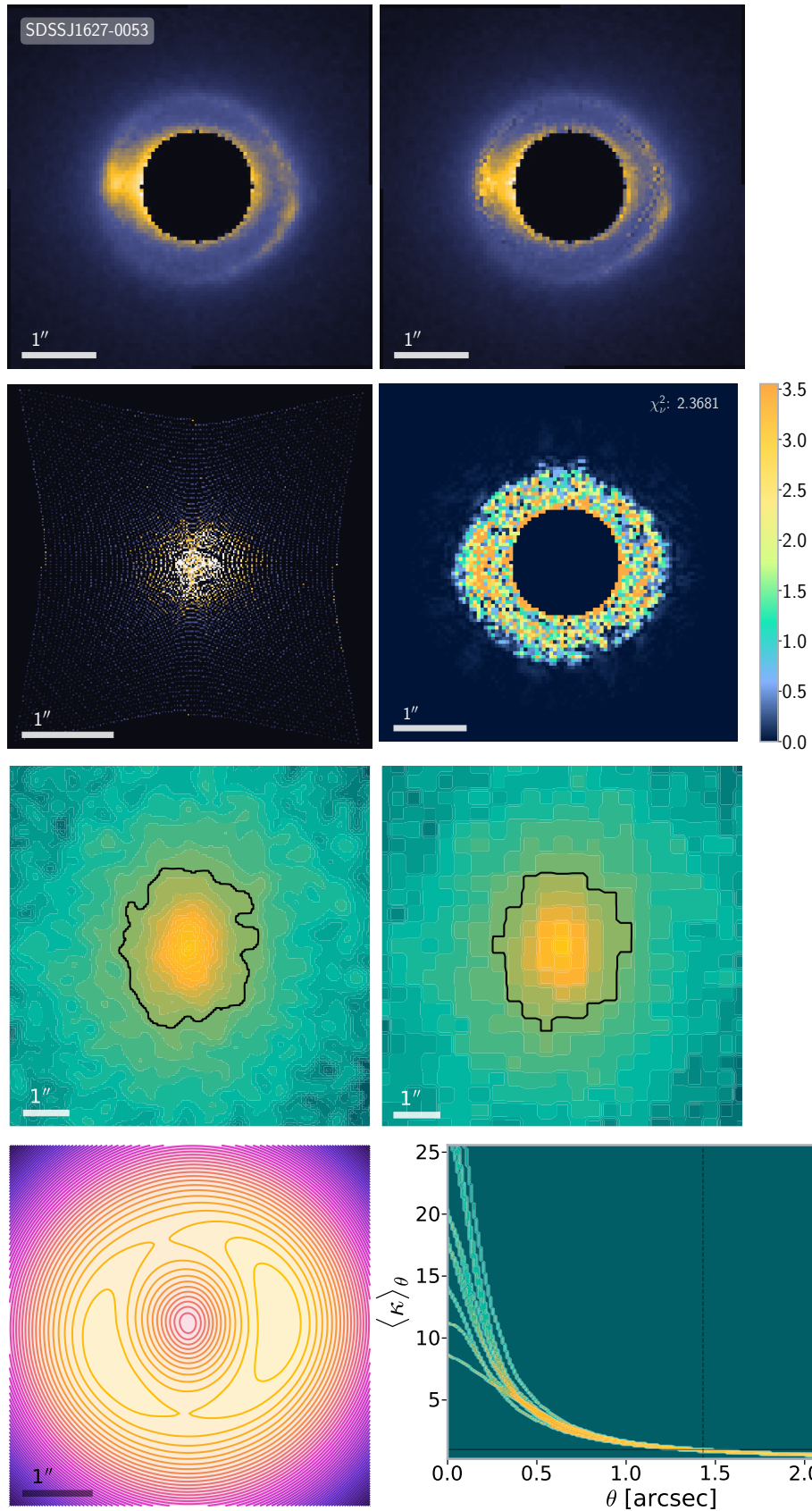


Figure 10. Results for SDSS J1627-0053. See Section 5 for details.